

# Dual-domain Multi-path Self-supervised Diffusion Model for Accelerated MRI Reconstruction

Yuxuan Zhang, Jinkui Hao, Bo Zhou

**Abstract**—Magnetic resonance imaging (MRI) is a vital diagnostic tool, but its inherently long acquisition times reduce clinical efficiency and patient comfort. Recent advancements in deep learning, particularly diffusion models, have improved accelerated MRI reconstruction. However, existing diffusion models’ training often relies on fully sampled data, models incur high computational costs, and often lack uncertainty estimation, limiting their clinical applicability. To overcome these challenges, we propose a novel framework, called Dual-domain Multi-path Self-supervised Diffusion Model (DMSM), that integrates a self-supervised dual-domain diffusion model training scheme, a lightweight hybrid attention network for the reconstruction diffusion model, and a multi-path inference strategy, to enhance reconstruction accuracy, efficiency, and explainability. Unlike traditional diffusion-based models, DMSM eliminates the dependency on training from fully sampled data, making it more practical for real-world clinical settings. We evaluated DMSM on two human MRI datasets, demonstrating that it achieves favorable performance over several supervised and self-supervised baselines, particularly in preserving fine anatomical structures and suppressing artifacts under high acceleration factors. Additionally, our model generates uncertainty maps that correlate reasonably well with reconstruction errors, offering valuable clinically interpretable guidance and potentially enhancing diagnostic confidence.

**Index Terms**—Diffusion Model, Accelerated MRI, Self-supervision, Lightweight Model, Uncertainty Estimation

## I. INTRODUCTION

MAGNETIC resonance imaging (MRI) is a widely used imaging technique for disease diagnosis and treatment planning. However, the inherently lengthy acquisition times associated with MRI pose significant challenges in clinical practice. Prolonged scan times can compromise patient comfort, increase motion-related artifacts, and limit patient throughput, hindering the overall efficiency of healthcare systems [1]. This is because data samples of an MR image are acquired sequentially in k-space and the speed at which k-space can be traversed is limited by physiological and hardware constraints. To address this, the field has turned to accelerated MRI techniques, which aim to use undersampling of k-space data to reconstruct high-quality MRI.

While undersampling in k-space contravenes the Nyquist-Shannon theorem, leading to aliasing artifacts in image reconstruction with traditional reconstructions, a line of different reconstruction algorithms have been proposed to reconstruct

high-quality MRI from accelerated scenarios, including Compress Sensing (CS)-based methods and Deep Learning (DL)-based methods. In recent years, DL-based approaches have shown significant improvements in reconstruction accuracy and efficiency over the CS-based approaches, especially under highly accelerated acquisition settings [2]. In early DL-based MRI reconstruction, convolutional neural networks (CNNs) and transformers were widely adopted to mitigate artifacts from undersampled data. For example, Yang et al. [3] proposed ADMM-Net, integrating the ADMM optimization framework with CNNs to bridge model-based and data-driven reconstruction. Schlemper et al. [4] introduced a cascaded CNN architecture to progressively refine MRI images, balancing reconstruction speed and quality. Generative Adversarial Networks (GANs) further advanced the field recently by learning implicit image priors [5]–[8]. For instance, Yang et al. [5] developed DAGAN, a conditional GAN incorporating U-Net generators and frequency-domain constraints for real-time reconstruction. Mardani et al. [7] enhanced structural preservation through cyclic consistency in GAN-based frameworks. However, CNNs and GANs remain limited by local receptive fields and training instability. To address these issues, transformer-based architectures emerged, leveraging self-attention for global context modeling. For instance, Huang et al. [9] designed SwinMR with hierarchical Swin transformer blocks to capture long-range dependencies efficiently. Zhou et al. [10] proposed DSFormer, a dual-domain transformer exploiting inter-modality correlations in both image and k-space domains. Despite their advantages, transformers incur high computational costs due to quadratic attention complexity.

Recently, diffusion model has gained significant attention for their ability to produce high-quality, highly detailed images [11]. In the accelerated MRI domain, these models have been adapted to address various reconstruction challenges through diverse approaches. In methods leveraging diffusion-based priors, Jiang et al. [12] introduce AdaDiff, which employs adaptive diffusion priors through an unconditional generative image prior and a two-phase reconstruction approach, achieving robust and high-quality reconstructions. Similarly, Guan et al. [13] propose the Correlated and Multi-Frequency Diffusion Model (CM-DM), utilizing multi-frequency priors to constrain noise distributions and improve convergence efficiency, effectively balancing noise suppression and detail preservation. While these approaches demonstrate the power of incorporating explicit priors, their performance may depend on the quality and generality of the prior assumptions. To address this limitation, recent studies have explored methods that focus instead on optimizing reconstruction directly in the

Y. Zhang is with the Department of Radiology, Northwestern University, Chicago, IL, 60611, USA, and the Department of Biomedical Engineering, Huazhong University of Science and Technology, Wuhan, China. J. Hao and B. Zhou are with the Department of Radiology, Northwestern University, Chicago, IL, 60611, USA. Corresponding email: bo.zhou@northwestern.edu

single domain. For example, in the image domain, Ozturkler et al. [14] develop a regularized 3D diffusion model combined with an optimization method for 3D MRI reconstruction, enhancing image quality and reducing noise without requiring strong prior constraints. Additionally, Geng et al. [15] propose DP-MDM, a detail-preserving framework that employs multiple diffusion models to extract structural and high-frequency features, significantly improving the recovery of fine anatomical details for diagnostic applications. While these methods focus on the image domain reconstruction, diffusion model also shows promising results in the k-space domain. For example, Ravula et al. [16] explore the theoretical foundations of diffusion models for compressed sensing MRI, proposing a novel optimization strategy that embeds k-space projection operators into the reverse diffusion process.

Diffusion models have demonstrated remarkable potential for accelerated MRI reconstruction in generating high-quality, detailed images. However, there are three existing challenges from the prior works in this domain. First, these previous diffusion model methods typically rely on supervised learning, requiring fully-sampled paired datasets that are difficult to obtain in clinical settings [4], [17]–[22]. This dependency limits their practical applicability, especially in scenarios where fully-sampled data is scarce or unavailable. Although there are several related self-supervised methods proposed recently [10], [23]–[26], they usually only focus on single-domain reconstruction (e.g., k-space only), therefore resulting in suboptimal reconstructions. In addition, these methods are typically developed for traditional CNN architectures. Second, many previous diffusion models implement transformers and their variants with heavy self-attention computation mechanisms as the backbone of the diffusion model to achieve enhanced reconstruction performance. However, these implementations are typically large and heavy, thus requiring substantial computational and memory costs. Lastly, these methods typically lack mechanisms for uncertainty estimation, which is critical for explainability and clinical decision-making.

To address these limitations, we propose a Dual-domain Multi-path Self-supervised Diffusion Model (DMSM) for accelerated MRI reconstruction with three key innovations. **Dual-domain Self-supervised Diffusion Model:** We design a dual-domain self-supervised training method for diffusion models that allows training without using paired fully sampled MRI data. **Light-weight network for diffusion model:** We develop a lightweight time-index-aware hybrid-attention network in the diffusion model which aims for high-quality MRI reconstruction while reducing the computational and time burdens. **Multi-path Uncertainty Estimation:** We propose a novel multi-path sampling strategy in DMSM to further enhanced reconstruction quality while enabling uncertainty estimation. Our experimental results on two large-scale MRI datasets show that our method can reconstruct high-quality high-fidelity MRI with training only from under-sampled MRI data and enable uncertainty estimation that correlates reasonably well with the true error.

## II. METHODS

The overall architecture of our proposed model is illustrated in Figure 1. There are three key components in our model: dual-domain self-supervised diffusion model (II-A1), light-weight hybrid attention network for reconstruction diffusion model (II-B1), and multi-path diffusion model inference strategy (II-A2).

In this section, we also explain the detailed implementation of DMSM (II-C), experimental datasets (II-C), baseline methods for comparison (II-D), and evaluation metrics (II-D).

### A. Dual-domain Multi-path Self-supervised Diffusion Model

In DMSM, we consider the scenario where a conditional diffusion model needs to be trained for accelerated MRI reconstruction. Instead of fully supervised training, DMSM uses a customized dual-domain self-supervised learning strategy only requires under-sampled data. Once trained, the diffusion model can be used for multi-path inference for reconstruction prediction and uncertain estimation. In the following, we discuss the details of our training and inference designs in DMSM.

1) *Dual-Domain Self-Supervised Training:* During training, we employ a partition mask strategy. This approach randomly divides the input under-sampled k-space  $y_u$  into two distinct partitions, denoted as  $y_{u,p1}$  and  $y_{u,p2}$ :

$$y_{u,p1} = M \odot y_u, \quad (1)$$

$$y_{u,p2} = (1 - M) \odot y_u. \quad (2)$$

where  $M$  is a binary undersampling mask applied to  $y_u$ . Then,  $y_u$ ,  $y_{u,p1}$ , and  $y_{u,p2}$  are inputted into three identical diffusion models where the models' weights are shared during training. In each diffusion model, in the forward diffusion process, we gradually add Gaussian noise based on a variance schedule  $\beta_t = \beta_1, \dots, \beta_T$  to  $x_0$  (at time step  $T = 0$ ) where  $x_0$  is an initially reconstructed under-sampled MR image  $x_u$  converted from  $y_u$ :

$$q(x_t|x_{t-1}) = \mathcal{N}\left(x_t; \sqrt{1 - \beta_t}x_{t-1}, \beta_t I\right) \quad (3)$$

Then, our backward diffusion process is applied to gradually remove noise from a pure Gaussian distribution  $x_T$  to reconstruct  $x_0$  using a denoising reconstruction neural network:

$$p_\theta(x_{t-1}|x_t) = \mathcal{N}\left(x_{t-1}; \epsilon_\theta(x_t, t), \tilde{\beta}_t I\right) \quad (4)$$

where  $\tilde{\beta}_t = \frac{1 - \bar{\alpha}_{t-1}}{1 - \bar{\alpha}_t} \beta_t$  and  $\epsilon_\theta$  represents the denoising neural network parametrized during backward diffusion. And the diffusion model can be trained using the following loss:

$$\mathcal{L}_{DM} := \mathbb{E}_{t,x_0,\epsilon,y_u} \left[ \|\epsilon_t - \epsilon_\theta(x_t, t, y_u)\|^2 \right] \quad (5)$$

where  $\bar{\alpha}_t = \prod_{m=1}^t \alpha_m$ ,  $\alpha_t = 1 - \beta_t$  and  $\epsilon \sim \mathcal{N}(0, I)$ . In this particular task, our reverse diffusion steps are parameterized with an LHAN+DC based backbone network (Figure 1 and to be detailed later).

Then, our self-supervised losses come from two sources, including image-domain self-supervision and frequency-domain self-supervision for the diffusion model. For the first one, the

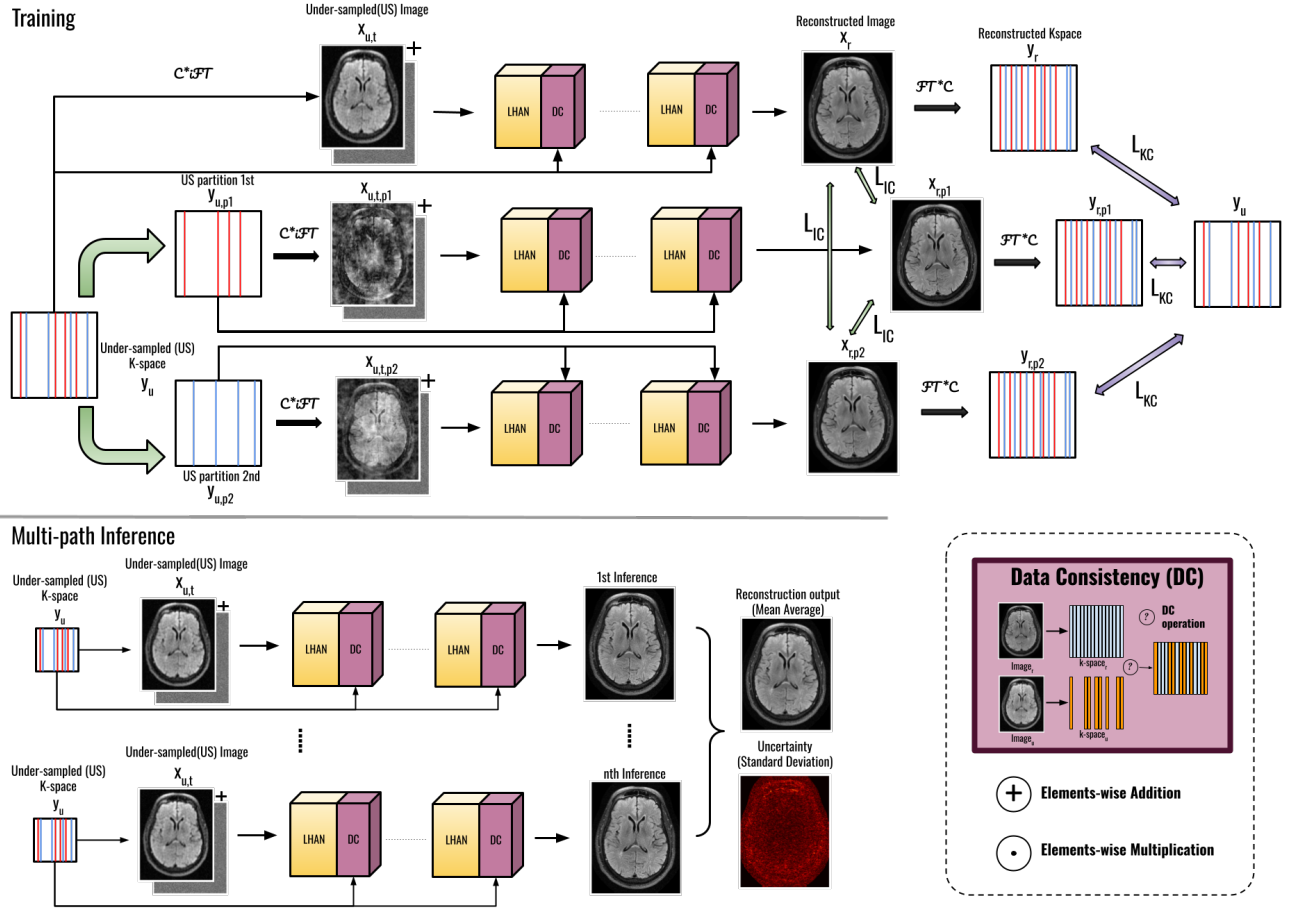


Fig. 1. Overview of the Dual-Domain Multi-Path Self-Supervised Diffusion Model (DMSM). During training, the original under-sampled k-space  $y_u$  is randomly divided into 2 partitions  $y_{u,p1}$  and  $y_{u,p2}$ . The training process takes  $y_u, y_{u,p1}, y_{u,p2}$  as inputs, and the self-supervised loss is performed on image domain  $\mathcal{L}_{IC}$  and k-space domain  $\mathcal{L}_{KC}$  for the diffusion model. Once trained, the diffusion model reconstructs MR images multiple times to get the final output and uncertainty.

loss aims to minimize the difference between the diffusion model reconstruction from all three different under-sampled data from the same patient input, thus is defined as:

$$\mathcal{L}_{IC} = \|\hat{x}_r - \hat{x}_{r,p1}\| + \|\hat{x}_r - \hat{x}_{r,p2}\| + \|\hat{x}_{r,p1} - \hat{x}_{r,p2}\| \quad (6)$$

where  $\hat{x}_r, \hat{x}_{r,p1}, \hat{x}_{r,p2}$  are the final outputs of our DMSM reconstruction network  $R_\theta$ :

$$\hat{x}_r = R_\theta(x_{u,t}, y_u, M, C, t) \quad (7)$$

$$\hat{x}_{r,p} = R_\theta(x_{u,t,p}, y_{u,p}, M, C, t) \quad (8)$$

where  $t$  is the time-index and  $C$  is the coil sensitivities map.  $x_{u,t}$  is the under-sampled image with scheduled noise added, and  $x_{u,t,p}$  is the one from the partitions:

$$x_{u,t} = \sqrt{\alpha_t}x_u + \sqrt{1 - \alpha_t}\epsilon \quad (9)$$

For the frequency domain self-supervision, the loss is formulated as:

$$\mathcal{L}_{KC} = \|\hat{y}_r - y_u\| + \|\hat{y}_{r,p1} - y_u\| + \|\hat{y}_{r,p2} - y_u\| \quad (10)$$

where  $\hat{y}_{r,p1}$  and  $\hat{y}_{r,p2}$  are reconstructed k-space from different partitions (i.e.  $\hat{x}_{r,p1}$  and  $\hat{x}_{r,p2}$ ).

Combining all the loss objectives above, our final training loss function can be formulated as:

$$\mathcal{L} = \lambda_{IC} * \mathcal{L}_{IC} + \lambda_{KC} * \mathcal{L}_{KC} + 3 * \mathcal{L}_{DM} \quad (11)$$

where  $\lambda_{IC} = 1$  and  $\lambda_{KC} = 5$  were set empirically to achieve stable training process.

2) *Multi-Path Inference*: Once the diffusion model is trained using the above pipeline, we propose a multi-path inference strategy that inference the trained diffusion model with different random noise initiations, generating multiple outputs for a single test data sample. The averaged output is used for enhanced prediction and the standard deviation is used for uncertainty estimation. The overall inference procedure is illustrated in Figure 1. Specifically, the reverse diffusion step at time-index  $t$  is given by:

$$x_{t-1} = R_\theta(x_t, y_t^\epsilon, M, C, t) + \sigma_t z \quad (12)$$

$$y_t^\epsilon = \mathcal{F}(\sqrt{\alpha_t}x_u + \sqrt{1 - \alpha_t}\epsilon_{low}) \quad (13)$$

where  $\epsilon_{low} \sim \mathcal{N}(0, 0.1I)$  and  $z \sim \mathcal{N}(0, I)$ . Let the  $N$  independent outputs from the multiple inference paths be denoted as  $\hat{x}_1, \hat{x}_2, \dots, \hat{x}_N$ . The average output  $\hat{x}_{avg}$  and the

standard deviation  $\sigma_{\hat{x}}$  across these outputs can be computed as:

$$\hat{x}_{avg} = \frac{1}{N} \sum_{i=1}^N \hat{x}_i \quad (14)$$

$$\sigma_{\hat{x}} = \sqrt{\frac{1}{N} \sum_{i=1}^N (\hat{x}_i - \hat{x}_{avg})^2} \quad (15)$$

where  $\hat{x}_{avg}$  represents the averaged reconstructed image and  $\sigma_{\hat{x}}$  gives the uncertainty (standard deviation) of the outputs.

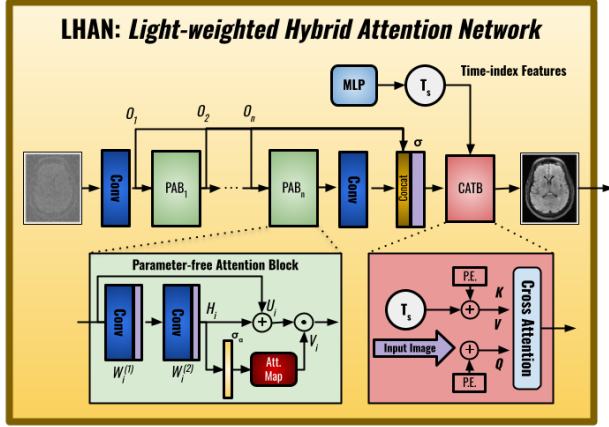


Fig. 2. Architecture of Light-weighted Hybrid Attention Network (LHAN) in DMSM (Figure 1). It consists of multiple Parameter-free Attention Blocks (PABs) and a Cross-Attention Transformer Block (CATB). The PABs enable MRI reconstruction feature extraction, while CATB fuse time index and the extract feature. The output of LHAN is then inputted into the DC layer.

### B. Backbone Networks in DMSM

For the backbone of our diffusion model, we develop a Light-weighted Hybrid Attention Network (LHAN), to efficiently generate high-quality reversed images. Then, it is followed by a Data Consistency (DC) Layer to ensure that the reconstructed k-space is consistent with the measured data throughout the reverse process.

1) *Light-weighted Hybrid Attention Network*: The LHAN architecture consists of multiple Parameter-free Attention Blocks (PABs), and followed by a Cross-Attention Transformer Block (CATB). The PABs are responsible for extracting features with attention to recovering the MRI structures, while the CATB aims to integrate time-indexed embeddings with the PAB features. Specifically, each PAB includes 2 convolution layers for feature extraction and a symmetric activation function for parameter-free attention computation. Given a feature map input  $O_{i-1}$ , the process can be described as follows:

$$H_i = \sigma(W_i^{(2)} \star \sigma(W_i^{(1)} \star O_{i-1})), \quad (16)$$

where  $W_i^{(1)}, W_i^{(2)}$  are two independent convolutional layers,  $\star$  represents convolution, and  $\sigma$  is the sigmoid activation function. Then, the attention weight  $V_i$  is calculated by applying  $\sigma_a$  to the initial extracted feature  $H_i$  by:

$$V_i = \sigma_a(H_i), \quad (17)$$

where  $\sigma_a$  is the symmetric activation function of the original one  $\sigma$ , which is set to be  $Sigmoid(x) - 0.5$ . The symmetry of  $\sigma_a$  ensures equal emphasis on positive or negative gradients (e.g., edge directions), while its monotonicity amplifies regions with rich textures, thus generating attention without parameters. Then, the attention  $V_i$  is applied to  $U_i = O_{i-1} \oplus H_i$  by:

$$O_i = U_i \odot V_i, \quad (18)$$

where  $\oplus$  denotes element-wise addition. For the overall process,  $O_i$  represents the feature map at each PAB's input or output. After 5 PABs, the final feature map  $O_n^t$  is obtained by concatenating features from specific PABs, followed by a convolutional layer.  $O_n^t$  then performs as input into CATB, which captures latent features associated with the time-index  $w_i^t$  obtained from our Time-index Network.

The Time-index Network takes the time index of the diffusion model, denoted as  $t$ , as input. It is processed by a Multilayer Perceptron (MLP) network consisting of 12 fully-connected layers, with 32 neurons in each layer. The output of the MLP is a latent vector, which is used to compute cross-attention. Let the time index be represented by  $t$ , and the input image at time step  $t$  be denoted as  $x_t$ . The MLP network processes the time index to produce a latent feature  $w_i^t$ :

$$w_i^t = \text{MLP}(t) \quad (19)$$

where  $w_i^t \in \mathbb{R}^{32}$  is the output latent vector with 32 dimensions, and the MLP function applies a series of transformations through 12 fully connected layers.

The CATB takes the reconstructed image features and time-index latent features as inputs and computes their weighted importance through cross-attention transformer-based network.

$$att^t = \text{softmax} \left( \frac{Q(O_n^t + P.E.) K (w_i^t + P.E.)^T}{\sqrt{n}} \right) V (w_i^t), \quad (20)$$

$$O_c^t = \alpha(att) \odot \left( \frac{O_n^t - \mu(O_n^t)}{\sigma(O_n^t)} \right). \quad (21)$$

This weighted representation is combined with the original features using a residual connection,

$$x_{\text{output}}^t = O_c^t \oplus O_n^t \quad (22)$$

2) *DC Layer*: The DC Layer operates within our backbone architecture. After each reverse diffusion step, the DC Layer projects the current estimate of the reconstructed image back into k-space to ensure consistency with the acquired data. This is achieved through the following operation:

$$x_{\text{output}}^t = \mathcal{F}^{-1} \{ \mathcal{F}(C x_{\text{output}}^t) \odot (1 - M_p) + \mathcal{F}(C x_u) \odot M_p \} \quad (23)$$

This operation combines the current image estimate with the actual k-space data, ensuring consistency with the measured data while allowing the model to learn the underlying image structure from the undersampled data.

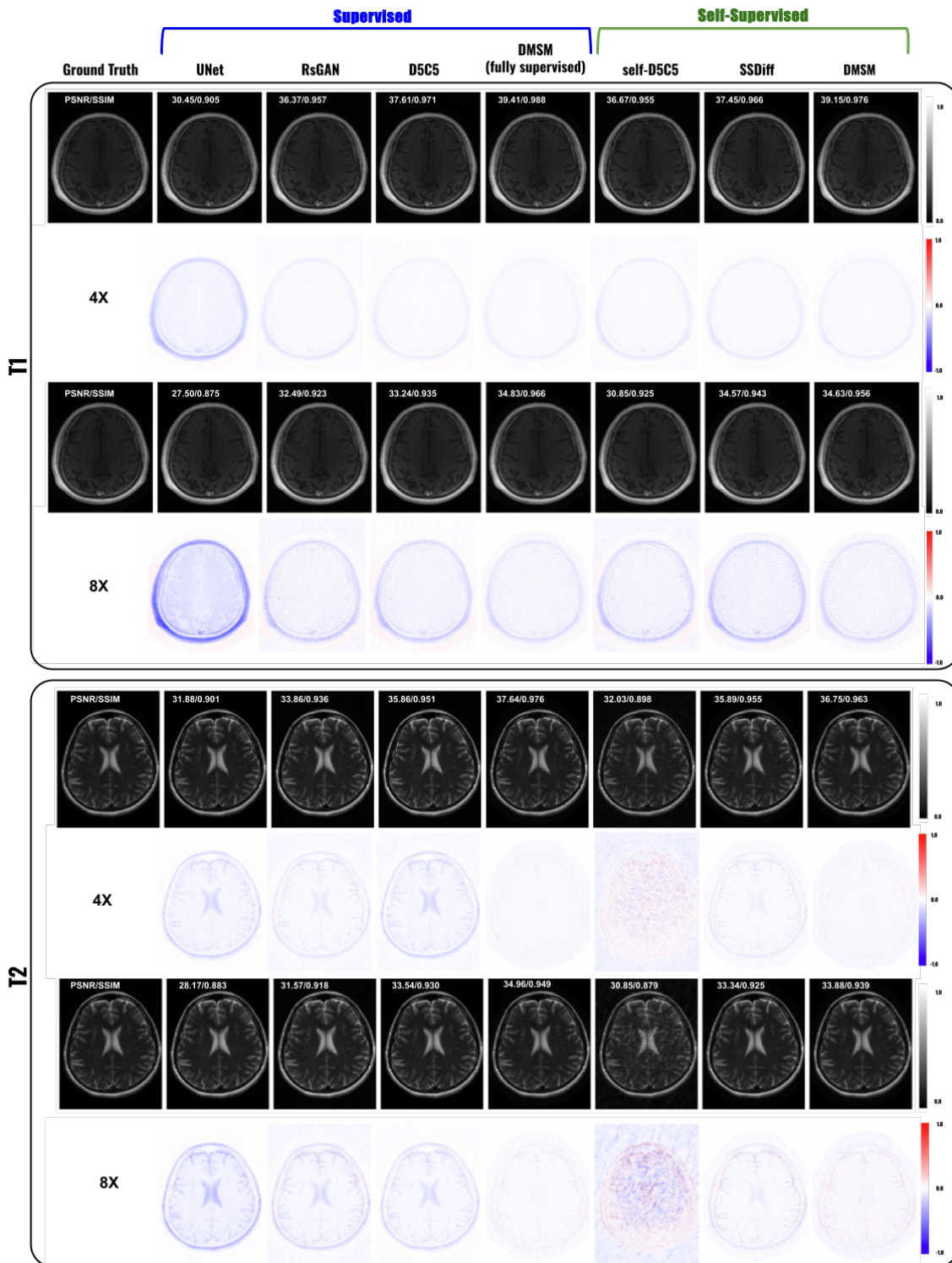


Fig. 3. T1(top) and T2(bottom) MRI reconstruction results on fastMRI dataset across all performed baseline methods. Two different acceleration settings (R=4 and R=8) are included. The corresponding error maps are shown right below each reconstruction visualization. Closer to white indicates a better reconstruction compared to the ground truth. PSNR and SSIM values are also reported on the top of the reconstruction results.

### C. Data Preparation and Implementation Details

We collected two public MRI datasets to evaluate the performance of our proposed method. The first dataset is the fastMRI brain dataset [27], which comprises data from 180 subjects. It was partitioned into training, validation, and

testing sets with 120, 10, and 50 subjects, respectively. During training, slices from all subjects were randomly shuffled and fed into the model as individual 2D samples. This ensures that our method is exposed to diverse anatomical variations across different slices, thereby enhancing its robustness for single-slice reconstruction. For each subject, it encompasses T1-, T2-,



TABLE I

QUANTITATIVE COMPARISONS OF RECONSTRUCTION RESULTS ON FASTMRI DATASET. RESULTS ON T1, T2, AND FLAIR WITH TWO HIGHLY ACCELERATED RATES ARE REPORTED, INCLUDING 4x AND 8x. THE BEST RESULTS ARE MARKED IN **BOLD**. THE FULLY SUPERVISED APPROACH MEANS DMSM TRAINED IN A FULLY SUPERVISED MANNER WITH ACCESS TO PAIRED GROUND TRUTH. "†" INDICATES THAT THE DIFFERENCE BETWEEN DMSM AND ALL SUPERVISED AND SELF-SUPERVISED BASELINE METHODS ARE SIGNIFICANT AT  $p < 0.00001$  (BONFERRONI MULTIPLE COMPARISONS-ADJUSTED ALPHA LEVEL) BASED ON THE NON-PARAMETRIC WILCOXON SIGNED RANK TEST.

T1 Evaluation	4x			8x			# Parameters
	PSNR/dB	SSIM	MAE/*10 <sup>-3</sup>	PSNR/dB	SSIM	MAE/*10 <sup>-3</sup>	
UNet	30.45 ± 2.37	0.905 ± 0.003	1.45 ± 0.72	27.50 ± 3.17	0.875 ± 0.003	3.60 ± 1.50	1.34M
D5C5	37.61 ± 2.34	0.971 ± 0.002	0.23 ± 0.47	31.24 ± 3.16	0.945 ± 0.002	1.70 ± 0.44	0.3M
RsGAN	36.37 ± 2.34	0.957 ± 0.002	0.55 ± 0.45	30.49 ± 3.13	0.913 ± 0.002	1.63 ± 0.43	11.3M
self-D5C5	36.67 ± 2.34	0.955 ± 0.002	0.47 ± 0.39	30.85 ± 3.13	0.925 ± 0.002	2.56 ± 0.73	0.3M
SSDiff	37.45 ± 2.35	0.966 ± 0.002	0.25 ± 0.10	34.57 ± 3.14	0.943 ± 0.002	0.49 ± 0.14	3.3M
Ours	<b>39.15 ± 2.95</b> †	<b>0.976 ± 0.021</b> †	<b>0.16 ± 0.10</b> †	<b>34.63 ± 3.16</b> †	<b>0.956 ± 0.003</b> †	<b>0.35 ± 0.10</b> †	0.8M
Fully supervised	39.41 ± 2.35	0.988 ± 0.002	0.12 ± 0.04	34.83 ± 3.13	0.966 ± 0.002	0.29 ± 0.10	0.8M
T2 Evaluation	4x			8x			# Parameters
	PSNR/dB	SSIM	MAE/*10 <sup>-3</sup>	PSNR/dB	SSIM	MAE/*10 <sup>-3</sup>	
UNet	31.88 ± 2.34	0.901 ± 0.004	4.8 ± 0.47	28.17 ± 2.82	0.883 ± 0.004	1.01 ± 0.40	1.34M
D5C5	35.86 ± 2.54	0.951 ± 0.003	0.28 ± 0.11	33.54 ± 2.46	0.930 ± 0.004	0.52 ± 0.21	0.3M
RsGAN	33.86 ± 2.98	0.936 ± 0.003	0.48 ± 0.10	31.57 ± 3.25	0.918 ± 0.003	0.71 ± 0.32	11.3M
self-D5C5	32.03 ± 2.34	0.898 ± 0.002	0.55 ± 0.45	30.85 ± 3.13	0.879 ± 0.002	1.63 ± 0.43	0.3M
SSDiff	35.89 ± 2.40	0.955 ± 0.011	0.31 ± 0.20	33.34 ± 2.46	0.925 ± 0.003	0.54 ± 0.21	3.3M
Ours	<b>36.75 ± 1.93</b> †	<b>0.963 ± 0.010</b> †	<b>0.23 ± 0.15</b> †	<b>33.88 ± 2.25</b> †	<b>0.939 ± 0.003</b> †	<b>0.46 ± 0.18</b> †	0.8M
Fully supervised	37.64 ± 2.24	0.976 ± 0.003	0.13 ± 0.04	34.96 ± 1.97	0.949 ± 0.003	0.30 ± 0.12	0.8M
FLAIR Evaluation	4x			8x			# Parameters
	PSNR/dB	SSIM	MAE/*10 <sup>-3</sup>	PSNR/dB	SSIM	MAE/*10 <sup>-3</sup>	
UNet	28.69 ± 2.78	0.839 ± 0.004	3.9 ± 0.52	25.80 ± 3.58	0.797 ± 0.007	3.10 ± 1.30	1.34M
D5C5	32.96 ± 2.75	0.925 ± 0.004	0.70 ± 0.41	30.85 ± 3.54	0.894 ± 0.006	0.93 ± 0.32	0.3M
RsGAN	31.94 ± 2.99	0.893 ± 0.003	0.89 ± 0.31	30.10 ± 3.32	0.877 ± 0.004	1.50 ± 0.51	11.3M
self-D5C5	30.63 ± 2.34	0.887 ± 0.002	0.55 ± 0.45	28.97 ± 3.13	0.823 ± 0.002	1.63 ± 0.43	0.3M
SSDiff	33.64 ± 2.53	0.932 ± 0.003	<b>0.63 ± 0.25</b>	30.90 ± 2.98	0.898 ± 0.003	0.81 ± 0.32	3.3M
Ours	<b>35.19 ± 2.44</b> †	<b>0.935 ± 0.002</b> †	0.68 ± 0.21†	<b>31.44 ± 2.54</b> †	<b>0.909 ± 0.004</b> †	<b>0.71 ± 0.31</b> †	0.8M
Fully supervised	35.39 ± 2.94	0.940 ± 0.003	0.60 ± 0.21	32.54 ± 2.53	0.923 ± 0.005	0.55 ± 0.21	0.8M

and FLAIR-weighted acquisitions. To mitigate computational complexity, we employed the Generalized Coil Compression (GCC) technique to reduce the number of coils from the original dataset to five, consistent with previous works [28]. The image resolution is 512 × 512. The second dataset, IXI [29], is a simulated single-coil brain MRI dataset, which includes 30 subjects for training, 5 for validation, and 15 for testing. Similar here, each subject contains T1-, T2-, and PD-weighted acquisitions. The image resolution is 256 × 256. To simulate the clinical scenario of accelerated MRI, we retrospectively under-sampled the acquisitions using variable-density masks. These masks were generated based on a 2D Gaussian distribution, with variance adjusted to achieve acceleration rates of  $R = [4, 8]$ , reflecting the undersampling factors used in our experiments.

We implemented our method in Tensorflow and performed experiments using an NVIDIA GeForce RTX 4090 GPU. We train all models with a batch size of 1 for 500k training steps. The Adam solver was used to optimize our models with  $lr = 1 \times 10^{-5}$ ,  $\beta_1 = 0.9$ , and  $\beta_2 = 0.999$ .

#### D. Evaluation Strategies and Baselines

We evaluate the reconstruction performance using Peak-Signal-to-Noise-Ratio (PSNR), Structural-Similarity-Index (SSIM), and Mean-Absolute-Error (MAE) between

reconstructions and the ground truth images (i.e. fully-sampled reconstruction). For the uncertainty estimation evaluation, we use Pearson correlation coefficients (PCC) to calculate the similarity between pixel-wise absolute errors (against fully-sampled ground truth) and our uncertainty estimation from the multi-path inference. For comparative evaluation, we compared our results with several baselines, including supervised baselines such as UNet [19], D5C5 [30], RsGAN [31] and self-supervised methods such as self-D5C5, SSDiff [32]. Notably, self-D5C5 is a self-supervised model-based reconstruction method that is trained only on under-sampled MRI data based on SSDU [24]. The hyperparameters and network architecture are the same as in D5C5. We also compared our DMSM with a fully-supervised strategy version which is trained with ground truth data.

### III. RESULTS

#### A. Experimental Results

The visual comparison between our DMSM and other previous methods under different acceleration settings is illustrated in Figure 3 and 4. In T1-weight reconstruction, as shown in the top panel of Figure 3, the UNet-based reconstruction exhibited substantial discrepancies from the ground truth. While supervised methods such as RsGAN and D5C5 demonstrated notable visual improvements, their performances

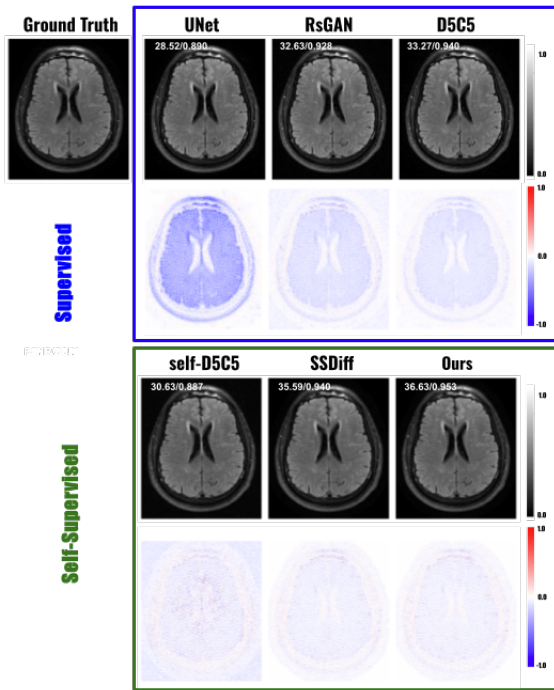


Fig. 4. PD MRI reconstruction results on IXI dataset across all performed baseline methods. 4× acceleration results are presented. The corresponding error maps are shown right below each reconstruction. Closer to white indicates a better reconstruction compared to the ground truth. PSNR and SSIM values are also reported on the top of the reconstruction results.

diverged in specific aspects. The RsGAN-generated images achieved perceptually enhanced contrast but introduced excessive background noise, leading to degraded quantitative metrics. Replacing D5C5 with a self-supervised paradigm resulted in unstable reconstructions plagued by introducing artifacts and spatial distortions. In contrast, the recently proposed SSDiff method effectively recovered subtle anatomical structures, yet our DMSM framework achieved superior performance, particularly excelling in preserving edge sharpness and intensity homogeneity. Under the more challenging R=8 acceleration setting, the limitations of the baseline methods became even more apparent. We noticed that the self-D5C5 failed to produce reliable results, with reconstructions dominated by structural distortions. SSDiff showed reduced performance compared to the R=4 case, with noticeable intensity drifts in fluid-filled regions. However, DMSM consistently delivered high-quality reconstructions. Similar trends were observed on T2-weighted fastMRI and PD IXI datasets.

The quantitative results for fastMRI and IXI are summarized in Table I and Table II. Consistent with our observations from the visualization results, our method achieves the best overall performance across all test samples on average. For instance, under the x4 acceleration setting for T1-weighted imaging, our method attains a PSNR of 39.15 dB, outperforming the previous best method, SSDiff, by approximately 1.7 dB. Additionally, the MAE is reduced by 54.5%. Under the more challenging x8 acceleration setting, similarly, our method surpasses SSDiff in MAE by 28.6%. A similar trend

TABLE II  
QUANTITATIVE COMPARISONS OF RECONSTRUCTIONS ON IXI DATASET. RESULTS ON T1, T2, AND PD WITH TWO DIFFERENT ACCELERATED RATES ARE REPORTED, INCLUDING 4× AND 8×. THE BEST RESULTS ARE MARKED IN **BOLD**. THE FULLY SUPERVISED APPROACH MEANS DMSM TRAINED IN A FULLY SUPERVISED MANNER WITH ACCESS TO PAIRED GROUND TRUTH. "†" INDICATES THAT THE DIFFERENCE BETWEEN DMSM AND ALL SUPERVISED AND SELF-SUPERVISED BASELINE METHODS ARE SIGNIFICANT AT  $p < 0.00001$ .

Evaluation	T1		
	PSNR/dB	SSIM	MAE/*10 <sup>-3</sup>
UNet	32.48 ± 3.49	0.934 ± 0.004	0.89 ± 0.32
D5C5	38.64 ± 3.34	0.978 ± 0.003	0.37 ± 0.19
RsGAN	37.84 ± 3.48	0.969 ± 0.003	0.55 ± 0.15
self-D5C5	37.69 ± 3.32	0.972 ± 0.003	0.40 ± 0.19
SSDiff	39.28 ± 3.20	0.980 ± 0.002	0.31 ± 0.07
Ours	<b>40.04 ± 3.72†</b>	<b>0.989 ± 0.008†</b>	<b>0.19 ± 0.04†</b>
Fully supervised	40.15 ± 2.85	0.988 ± 0.002	0.12 ± 0.04
Evaluation	T2		
	PSNR/dB	SSIM	MAE/*10 <sup>-3</sup>
UNet	30.25 ± 3.30	0.910 ± 0.004	1.20 ± 0.40
D5C5	36.15 ± 3.15	0.958 ± 0.003	0.48 ± 0.20
RsGAN	35.20 ± 3.20	0.945 ± 0.003	0.60 ± 0.25
self-D5C5	32.61 ± 3.29	0.922 ± 0.005	1.12 ± 0.29
SSDiff	36.98 ± 2.95	0.960 ± 0.002	0.42 ± 0.15
Ours	<b>38.75 ± 2.95†</b>	<b>0.970 ± 0.010†</b>	<b>0.30 ± 0.15†</b>
Fully supervised	39.15 ± 2.85	0.975 ± 0.003	0.20 ± 0.05
Evaluation	PD		
	PSNR/dB	SSIM	MAE/*10 <sup>-3</sup>
UNet	28.52 ± 3.20	0.890 ± 0.003	1.60 ± 0.65
D5C5	33.27 ± 3.55	0.940 ± 0.002	0.70 ± 0.24
RsGAN	32.63 ± 3.13	0.928 ± 0.002	0.63 ± 0.23
self-D5C5	30.63 ± 3.34	0.887 ± 0.003	0.37 ± 0.19
SSDiff	35.59 ± 3.14	0.940 ± 0.002	0.59 ± 0.19
Ours	<b>36.63 ± 3.16†</b>	<b>0.953 ± 0.003†</b>	<b>0.54 ± 0.10†</b>
Fully supervised	36.83 ± 3.13	0.964 ± 0.002	0.39 ± 0.10

is observed in the IXI results. Notably, compared to the fully supervised version of our method, which represents the ceiling performance when paired data is available, our self-supervised DMSM achieves the closest performance.

The number of parameters for each model is summarized in the last column of Table I to compare their computational burden. As shown, our model achieves the best performance with a compact size of only 0.8M parameters. While D5C5 has a smaller model size (0.3M) due to its use of only cascaded convolutional layers, our approach maintains a model size under 1M while nearly halving the MAE. Compared to the previous best model, SSDiff, we reduce the model size by nearly fivefold while simultaneously enhancing performance.

Figure 5 illustrates an example of DMSM’s uncertainty estimation and its correlation with reconstruction error (computed using ground truth). As we can see, the input suffers from artifacts due to accelerated acquisition, yet DMSM successfully generates high-quality reconstructions while providing uncertainty estimates that correlate well with the error (PCC = 0.58). The averaged PCC value between the uncertainty estimation and error is  $0.44 \pm 0.07$ ,  $0.37 \pm 0.11$ , and  $0.53 \pm 0.13$  for T1, T2, and FLAIR on fastMRI, respectively. Please note the default number of paths set here is 15.

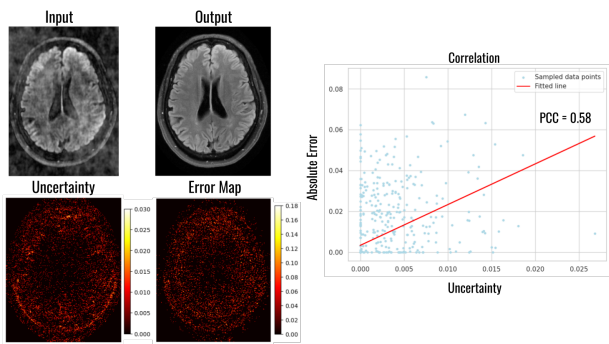


Fig. 5. Uncertainty estimation on the multi-path averaged reconstruction. A result of FLAIR contrast on the fastMRI dataset with  $4\times$  acceleration is shown. Brighter values indicate higher values of variance and bias.

TABLE III

QUANTITATIVE ANALYSIS ON UNCERTAINTY ESTIMATION OF DMSM USING THE FASTMRI DATASET. CORRELATION METRICS WITH DIFFERENT NUMBERS OF INFERENCE PATHS ARE REPORTED.

Correlation	T1	T2	FLAIR
N = 5	$0.38 \pm 0.10$	$0.35 \pm 0.11$	$0.43 \pm 0.17$
N = 10	$0.42 \pm 0.08$	$0.35 \pm 0.11$	$0.54 \pm 0.13$
N = 15	$0.44 \pm 0.07$	$0.37 \pm 0.11$	$0.53 \pm 0.13$

### B. Ablation Studies

**Impact of diffusion self-supervision across different domains:** To assess the effectiveness of our multi-domain self-supervised learning strategy for the diffusion model, we compared DMSM’s performance using only single-domain self-supervision. Figure 6 provides a visual comparison between models trained with only k-space self-supervision (2nd column) and those incorporating both k-space and image-domain self-supervision (last column). The results demonstrate that multi-domain self-supervision significantly improves reconstruction quality and reduces error. The quantitative comparison in Table IV further supports this observation, showing a performance drop from 38.15 dB to 36.39 dB when image-domain self-supervision is omitted. Notably, the model failed to converge when trained with image-domain self-supervision alone, underscoring the necessity of incorporating both domains for effective self-supervision. The results are not reported for image-domain self-supervision for this reason as well.

TABLE IV

ABLATION STUDIES OF DMSM WITH OR WITHOUT IMAGE DOMAIN CONSTRAINT DURING TRAINING (2ND ROW), WITH OR WITHOUT PABS (3RD ROW), WITH OR WITHOUT DC LAYER (4TH ROW). T1 ON FASTMRI DATASET IS USED FOR ANALYSIS HERE.

Metrics	PSNR/dB	SSIM	MAE/ $\ast 10^{-3}$
Ours	$39.15 \pm 2.95$	$0.976 \pm 0.021$	$0.16 \pm 0.10$
w/o $L_{IC}$	$36.39 \pm 3.17$	$0.958 \pm 0.037$	$0.33 \pm 0.22$
w/o PABs	$37.65 \pm 3.10$	$0.962 \pm 0.025$	$0.23 \pm 0.11$
w/o DC Layer	$28.82 \pm 3.94$	$0.870 \pm 0.040$	$1.50 \pm 0.55$

**Impact of Sub-Network Structure in DMSM:** The backbone network in DMSM comprises two key modules: LHAN and DC. Here, we extensively evaluate the contribution of each

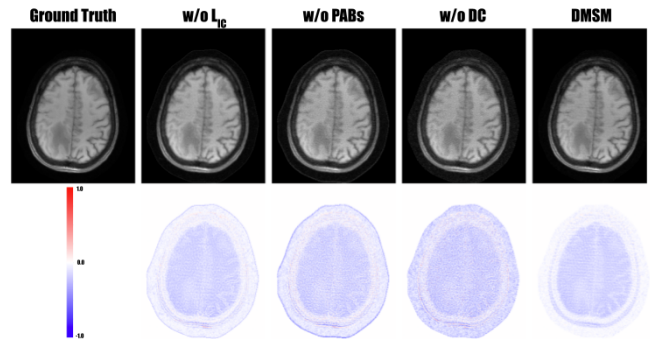


Fig. 6. Visualization of ablation studies on DMSM components. The DMSM reconstruction (top row) and the corresponding error map (bottom row) are shown. Results on excluding the image-domain loss (2nd column), LHAN (3rd column), and DC layer (4rd column) are visualized for a FLAIR example from fastMRI with  $4\times$  acceleration setting.

component. Figure 6 presents a visual comparison between reconstructions without PAB in LHAN (3rd column) and with PAB in LHAN (last column). As shown, PAB effectively extracts features using parameter-free attention, significantly reducing reconstruction error. Table IV and Figure 7 provide a detailed quantitative analysis of different numbers of PABs in LHAN. Performance is suboptimal without PAB (i.e., number of PAB = 0) but improves and converges when the number of PAB reaches to about 4. Additionally, we examine the impact of DC in the diffusion process. Both the visual examples in Figure 6 and the quantitative results in Table IV show that removing DC severely degrades performance, decreasing from 39.15 dB to 28.82 dB. This highlights the critical role of data consistency in ensuring effective diffusion-based reconstruction.

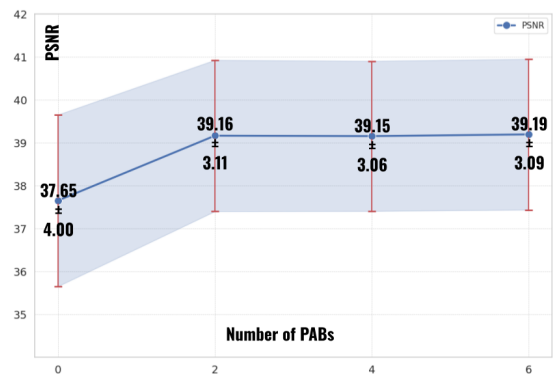


Fig. 7. Ablative study on using different numbers of PAB in LHAN. Please note that with the number of PAB equal to 0, only CATB was used.

**Impact of Multi-Path Inference Strategy:** The multi-path inference strategy simultaneously enhances reconstruction performance and enables uncertainty estimation. Here, we further investigate the effect of varying the number of inference paths in DMSM. Table V summarizes the reconstruction performance of DMSM across different path counts. As observed, increasing the number of paths consistently improves PSNR and SSIM, indicating enhanced reconstruction quality.



However, beyond  $N = 15$ , further gains become negligible, leading us to set  $N = 15$  as the default configuration. A similar trend is observed for uncertainty estimation. Table III shows that as the number of paths increases, the PCC between pixel-wise uncertainty estimation and error improves but converges around  $N = 15$ .

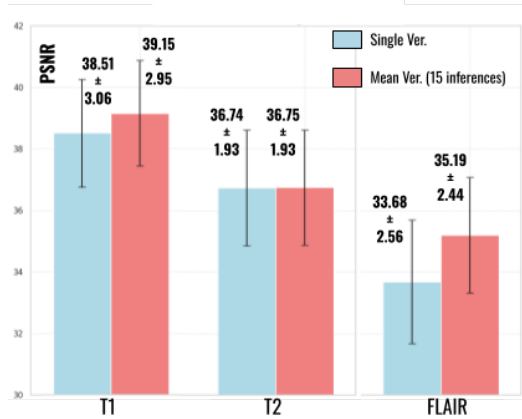


Fig. 8. Quantitative analysis on the reconstruction improvement from the multi-path inference. Consistent improvements from multi-path inference (red bar) to single-path inference (blue bar) are found for all sequences on fastMRI dataset under the  $4\times$  setting here.

TABLE V  
ABLATION STUDY RESULTS OF DMSM WITH DIFFERENT NUMBER OF INFERENCE PATHS. ANALYSIS WITH FASTMRI DATASET UNDER  $4\times$  ACCELERATION SETTING IS REPORTED.

PSNR/dB	T1	T2	FLAIR
$N = 5$	$38.65 \pm 3.06$	$36.74 \pm 1.92$	$34.35 \pm 2.58$
$N = 10$	$39.10 \pm 3.00$	$36.74 \pm 1.95$	$35.10 \pm 2.49$
$N = 15$	$39.15 \pm 2.95$	$36.75 \pm 1.93$	$35.19 \pm 2.44$

#### IV. DISCUSSION

In this work, we introduced DMSM, a lightweight diffusion-based reconstruction model trained using a dual-domain self-supervised strategy. Our approach enables high-quality MRI reconstruction while providing reliable uncertainty estimation. Our dual-domain self-supervised strategy leverages the complementary strengths of the image and k-space domains. By enforcing consistency between these domains, the model inherently respects the physical constraints of MRI acquisition while learning robust priors from undersampled data. Importantly, our approach relies solely on undersampled k-space data for both training and reconstruction, addressing a key limitation in clinical settings where fully sampled data is often unavailable. Building on this self-supervised framework, we developed a lightweight and efficient diffusion model tailored for MRI reconstruction. Our proposed backbone, which integrates a Lightweight Hybrid Attention Network (LHAN) with a Data Consistency (DC) module, enhances reconstruction accuracy while maintaining computational efficiency. Given a randomly noised undersampled MR image as input, LHAN extracts meaningful reconstruction features using attention mechanisms, while DC ensures consistency in the k-space

domain with the initial undersampled input. Within LHAN, we introduced a parameter-free symmetric activation function to compute attention maps, replacing traditional heavy self-attention mechanisms used in Transformer-based models. This design significantly reduces trainable parameters compared to baseline diffusion models. Additionally, the cross-attention module facilitates effective guidance from global latent variables (in our case, time-index features) at each diffusion step. Overall, this architecture balances high reconstruction quality with computational efficiency by integrating multi-scale and multi-domain information effectively. Furthermore, we implemented a multi-path inference strategy, which plays a crucial role in improving both reconstruction quality and interpretability. By leveraging a trained network to generate multiple reconstructions with subtle variations, we achieve consistent improvements in quantitative metrics. Additionally, uncertainty maps computed from these reconstructions exhibit a strong spatial correlation with error maps, highlighting regions of higher uncertainty. This feature enhances clinical interpretability by directing radiologists' attention to areas that may require closer inspection. Our experimental results demonstrate that DMSM is not only feasible but also highly competitive compared to both supervised and self-supervised reconstruction methods. The reconstructed MRI images exhibit superior visual fidelity and closer resemblance to ground truth (Figures 3 and 4). Additionally, DMSM outperforms prior methods in quantitative metrics, including PSNR, SSIM, and MAE (Tables I and II). The ablation studies further highlight the contributions of individual components, demonstrating their adaptability and effectiveness.

Despite its promising performance, our study has several limitations that warrant further exploration. First, while our dual-domain self-supervised strategy is theoretically applicable to general diffusion models, we validated it only within a conditional diffusion model framework. Future work could extend this approach to newer paradigms, such as the Bridge Diffusion Model [33], [34]. Second, our experiments were conducted on brain MRI datasets with limited contrasts (T1, T2, FLAIR, PD). Although the method is designed to be modality- and anatomy-agnostic, its generalizability to other anatomical regions (e.g., knee MRI) and MRI sequences remains unverified. Future work will explore its applicability to multi-organ and cross-modal reconstruction tasks. Another key limitation is that our evaluation focused primarily on image-level metrics using data from healthy subjects. To enhance clinical relevance, future studies should validate DMSM on pathological cases, such as tumor or lesion reconstruction. Incorporating radiologist assessments and testing on datasets with diverse pathologies will strengthen its potential for real-world deployment. Additionally, while our self-supervised framework eliminates dependence on fully sampled data, integrating a fine-tuning strategy could further improve performance. For instance, initializing the model with weights from a supervised variant (Section II-C) and fine-tuning it on unseen undersampled datasets may enhance adaptability to new acquisition protocols and hardware. Finally, the multi-path inference strategy, while beneficial for uncertainty estimation, increases inference time proportionally to the number of paths.

To mitigate this, future work could explore accelerated inference techniques such as progressive sampling strategies [35], [36] to reduce computational overhead without sacrificing reconstruction quality.

## V. CONCLUSION

We proposed a Dual-domain Multi-path Self-supervised Diffusion Model (DMSM) for accelerated MRI reconstruction, addressing key limitations of existing methods in fully-sampled data dependency, computational efficiency, and uncertainty estimation. Our method integrates dual-domain self-supervised training, a lightweight hybrid-attention network, and multi-path inference to achieve high-fidelity reconstructions. The experiment results demonstrate that DMSM achieves superior reconstruction quality compared to state-of-the-art supervised and self-supervised methods, with uncertainty maps potentially offering clinically interpretable guidance.

## REFERENCES

- [1] M. T. Vlaardingerbroek and J. A. Boer, *Magnetic resonance imaging: theory and practice*. Springer Science & Business Media, 2013.
- [2] J. Bernal, K. Kushibar, D. S. Asfaw, S. Valverde, A. Oliver, R. Martí, and X. Lladó, “Deep convolutional neural networks for brain image analysis on magnetic resonance imaging: a review,” *Artificial intelligence in medicine*, vol. 95, pp. 64–81, 2019.
- [3] Y. Yang, J. Sun, H. Li, and Z. Xu, “Admm-net: A deep learning approach for compressive sensing mri,” *arXiv preprint arXiv:1705.06869*, 2017.
- [4] J. Schlemper, J. Caballero, J. V. Hajnal, A. N. Price, and D. Rueckert, “A deep cascade of convolutional neural networks for dynamic mr image reconstruction,” *IEEE transactions on Medical Imaging*, vol. 37, no. 2, pp. 491–503, 2017.
- [5] G. Yang, S. Yu, H. Dong, G. Slabaugh, P. L. Dragotti, X. Ye, F. Liu, S. Arridge, J. Keegan, Y. Guo *et al.*, “Dagan: deep de-aliasing generative adversarial networks for fast compressed sensing mri reconstruction,” *IEEE transactions on medical imaging*, vol. 37, no. 6, pp. 1310–1321, 2017.
- [6] M. Mardani, E. Gong, J. Y. Cheng, S. S. Vasanawala, G. Zaharchuk, L. Xing, and J. M. Pauly, “Deep generative adversarial neural networks for compressive sensing mri,” *IEEE transactions on medical imaging*, vol. 38, no. 1, pp. 167–179, 2018.
- [7] T. M. Quan, T. Nguyen-Duc, and W.-K. Jeong, “Compressed sensing mri reconstruction using a generative adversarial network with a cyclic loss,” *IEEE transactions on medical imaging*, vol. 37, no. 6, pp. 1488–1497, 2018.
- [8] E. K. Cole, J. M. Pauly, S. S. Vasanawala, and F. Ong, “Unsupervised mri reconstruction with generative adversarial networks,” *arXiv preprint arXiv:2008.13065*, 2020.
- [9] J. Huang, Y. Fang, Y. Wu, H. Wu, Z. Gao, Y. Li, J. Del Ser, J. Xia, and G. Yang, “Swin transformer for fast mri,” *Neurocomputing*, vol. 493, pp. 281–304, 2022.
- [10] B. Zhou, N. Dey, J. Schlemper, S. S. M. Salehi, C. Liu, J. S. Duncan, and M. Sofka, “Dsformer: A dual-domain self-supervised transformer for accelerated multi-contrast mri reconstruction,” in *Proceedings of the IEEE/CVF winter conference on applications of computer vision*, 2023, pp. 4966–4975.
- [11] L. Yang, Z. Zhang, Y. Song, S. Hong, R. Xu, Y. Zhao, W. Zhang, B. Cui, and M.-H. Yang, “Diffusion models: A comprehensive survey of methods and applications,” *ACM Computing Surveys*, vol. 56, no. 4, pp. 1–39, 2023.
- [12] A. Güngör, S. U. Dar, Ş. Öztürk, Y. Korkmaz, H. A. Bedel, G. Elmas, M. Ozbey, and T. Çukur, “Adaptive diffusion priors for accelerated mri reconstruction,” *Medical image analysis*, vol. 88, p. 102872, 2023.
- [13] Y. Guan, C. Yu, Z. Cui, H. Zhou, and Q. Liu, “Correlated and multi-frequency diffusion modeling for highly under-sampled mri reconstruction,” *IEEE Transactions on Medical Imaging*, 2024.
- [14] B. Ozturkler, C. Liu, B. Eckart, M. Mardani, J. Song, and J. Kautz, “Smrd: Sure-based robust mri reconstruction with diffusion models,” in *International Conference on Medical Image Computing and Computer-Assisted Intervention*. Springer, 2023, pp. 199–209.
- [15] M. Geng, J. Zhu, X. Zhu, Q. Liu, D. Liang, and Q. Liu, “Dp-mdm: Detail-preserving mr reconstruction via multiple diffusion models,” *arXiv preprint arXiv:2405.05763*, 2024.
- [16] S. Ravula, B. Levac, A. Jalal, J. I. Tamir, and A. G. Dimakis, “Optimizing sampling patterns for compressed sensing mri with diffusion generative models,” *arXiv preprint arXiv:2306.03284*, 2023.
- [17] C. M. Hyun, H. P. Kim, S. M. Lee, S. Lee, and J. K. Seo, “Deep learning for undersampled mri reconstruction,” *Physics in Medicine & Biology*, vol. 63, no. 13, p. 135007, 2018.
- [18] M. A. Dedmari, S. Conjeti, S. Estrada, P. Ehses, T. Stöcker, and M. Reuter, “Complex fully convolutional neural networks for mr image reconstruction,” in *International Workshop on Machine Learning for Medical Image Reconstruction*. Springer, 2018, pp. 30–38.
- [19] S. Wang, Z. Su, L. Ying, X. Peng, S. Zhu, F. Liang, D. Feng, and D. Liang, “Accelerating magnetic resonance imaging via deep learning,” in *2016 IEEE 13th international symposium on biomedical imaging (ISBI)*. IEEE, 2016, pp. 514–517.
- [20] J. Sun, H. Li, Z. Xu *et al.*, “Deep admm-net for compressive sensing mri,” *Advances in neural information processing systems*, vol. 29, 2016.
- [21] C. Qin, J. Schlemper, J. Caballero, A. N. Price, J. V. Hajnal, and D. Rueckert, “Convolutional recurrent neural networks for dynamic mr image reconstruction,” *IEEE transactions on medical imaging*, vol. 38, no. 1, pp. 280–290, 2018.
- [22] B. Zhou and S. K. Zhou, “Dudornet: learning a dual-domain recurrent network for fast mri reconstruction with deep t1 prior,” in *Proceedings of the IEEE/CVF conference on computer vision and pattern recognition*, 2020, pp. 4273–4282.
- [23] A. Q. Wang, A. V. Dalca, and M. R. Sabuncu, “Neural network-based reconstruction in compressed sensing mri without fully-sampled training data,” in *Machine Learning for Medical Image Reconstruction: Third International Workshop, MLMIR 2020, Held in Conjunction with MICCAI 2020, Lima, Peru, October 8, 2020, Proceedings 3*. Springer, 2020, pp. 27–37.
- [24] B. Yaman, S. A. H. Hosseini, S. Moeller, J. Ellermann, K. Uğurbil, and M. Akçakaya, “Self-supervised physics-based deep learning mri reconstruction without fully-sampled data,” in *2020 IEEE 17th International Symposium on Biomedical Imaging (ISBI)*. IEEE, 2020, pp. 921–925.
- [25] B. Yaman, S. A. H. Hosseini, and M. Akçakaya, “Zero-shot self-supervised learning for mri reconstruction,” *arXiv preprint arXiv:2102.07737*, 2021.
- [26] B. Zhou, J. Schlemper, N. Dey, S. S. M. Salehi, K. Sheth, C. Liu, J. S. Duncan, and M. Sofka, “Dual-domain self-supervised learning for accelerated non-cartesian mri reconstruction,” *Medical Image Analysis*, vol. 81, p. 102538, 2022.
- [27] F. A. R. (FAIR) and N. L. Health, “fastmri: An open dataset and benchmarks for accelerated mri,” <https://github.com/maroomir/fastMRI>, 2024, accessed: 2025-02-12. [Online]. Available: <https://fastmri.med.nyu.edu/>
- [28] T. Zhang, J. M. Pauly, S. S. Vasanawala, and M. Lustig, “Coil compression for accelerated imaging with cartesian sampling,” *Magnetic resonance in medicine*, vol. 69, no. 2, pp. 571–582, 2013.
- [29] I. C. London and K. C. L. Guy’s Hospital, “Information extraction from images (ixi) dataset,” 2010, accessed: 2025-02-12. [Online]. Available: <http://brain-development.org/ixi-dataset/>
- [30] K. Kwon, D. Kim, and H. Park, “A parallel mr imaging method using multilayer perceptron,” *Medical physics*, vol. 44, no. 12, pp. 6209–6224, 2017.
- [31] S. U. Dar, M. Yurt, M. Shahdloo, M. E. Ildiz, B. Tınaz, and T. Çukur, “Prior-guided image reconstruction for accelerated multi-contrast mri via generative adversarial networks,” *IEEE Journal of Selected Topics in Signal Processing*, vol. 14, no. 6, pp. 1072–1087, 2020.
- [32] Y. Korkmaz, T. Cukur, and V. M. Patel, “Self-supervised mri reconstruction with unrolled diffusion models,” in *International Conference on Medical Image Computing and Computer-Assisted Intervention*. Springer, 2023, pp. 491–501.
- [33] B. Li, K. Xue, B. Liu, and Y.-K. Lai, “Bbmd: Image-to-image translation with brownian bridge diffusion models,” in *Proceedings of the IEEE/CVF conference on computer vision and pattern recognition*, 2023, pp. 1952–1961.
- [34] X. Su, J. Song, C. Meng, and S. Ermon, “Dual diffusion implicit bridges for image-to-image translation,” *arXiv preprint arXiv:2203.08382*, 2022.
- [35] T. Salimans and J. Ho, “Progressive distillation for fast sampling of diffusion models,” *arXiv preprint arXiv:2202.00512*, 2022.
- [36] C. Lu, Y. Zhou, F. Bao, J. Chen, C. Li, and J. Zhu, “Dpm-solver: A fast ode solver for diffusion probabilistic model sampling in around 10 steps,” *Advances in Neural Information Processing Systems*, vol. 35, pp. 5775–5787, 2022.